Numerical simulations of swirling pipe flows- decay of swirl and occurrence of vortex structures

H. A. Vaidya[1,2]**, Ö. Ertunç**[1,2]**, B. Genç**[1,2,3]**, F. Beyer**[1]**,
Ç. Köksoy**[1] **& A. Delgado**[1,2]

[1]Institute of Fluid Mechanics, FAU Erlangen-Nuremberg, Germany
[2]Erlangen Graduate School in Advanced Optical Technologies (SAOT), FAU
Erlangen-Nuremberg, Germany

E-mail: `haresh.vaidya@lstm.uni-erlangen.de`

Abstract. The present work aims at better understanding of the physics underlying swirling flows in pipes by means of numerical simulations. Direct numerical simulations have been carried out by using two different inlet swirl conditions. In one case, rotating honeycomb is used as the means to generate swirl whereas in the other case a solid body rotation is provided at the inlet. The inlet swirl intensity is varied in order to scan the underlying physics. Reynolds number 1730 is selected so that the flow remains in laminar regime. The results are compared with those obtained from the experiments using a similar experimental set-up. It is shown that the increase in the inlet swirl intensity leads to a faster decay of swirl downstream of the pipe. Similarly certain specific vortex structures are observed in the radial velocity contours. These structures are thought to be analogous with those found in the Taylor-Couette flow between a stationary outer cylinder and inner rotating cone. The reported investigations reveal dependence of swirl decay on the inlet swirl intensity and occurrence of vortex structures.

1. Introduction

Swirling flows are an important class of flows not only due to their complex nature but also due to their technical relevance in combustion, heat exchange, cyclone separation, mixing, etc. However, their complex nature hinders their modeling and thorough understanding (Jakirlic *et al.*, 2002). Due to this fact, swirling flows have been extensively studied for several decades and many publications can be found in the literature (see Steenbergen (1995); Rocklage-Marliani *et al.* (2003); Pashtrapanska *et al.* (2006) for detailed reviews) accordingly. These studies reveal the fact that, depending on the boundary conditions, swirling flows can undergo totally different scenarios and the flow field can exhibit different dynamical features. A great number of these studies concentrate on the effects of swirl when the swirling flow is created and subjected to gradual or sudden expansion in pipes or injected as a free jet (unconstrained) (Billant *et al.*, 1998; Novak & Sarpkaya, 2000; Facciolo *et al.*, 2007). In such flows, swirl component decays rapidly due to the action of adverse pressure gradient and sometimes vortex core breakdown phenomenon occurs (Novak & Sarpkaya, 2000). In contrast to these, present study concentrates on the relatively less studied case when the swirl is generated at the inlet of a straight circular pipe and constrained in it (Kitoh, 1991; Steenbergen, 1995; Rocklage-Marliani *et al.*, 2003; Genc

---

[3] Present address: CD-ADAPCO, Nordostpark 3 - 5, 90411 Nuremberg, Germany.

et al., 2005; Pashtrapanska *et al.*, 2006). In this kind of flow, the swirl component decays downstream of the pipe and as a consequence a number of different effects that have been reported; like stabilizing-destabilizing effect of swirl on turbulence (Kito, 1984), effect of swirl decay on breaking of axisymmetry (Pashtrapanska *et al.*, 2006), relaminarization of flow profile (Nishibory *et al.*, 1987), annihilation of Reynolds shear stresses (Rocklage-Marliani *et al.*, 2003). Genc *et al.* (2005, 2010) carried out experiments using rotating honeycomb for introducing swirl in a stationary circular pipe at a Reynolds number of 1730. The results highlight the influence of swirl on the flow field. The honeycomb introduces a solid body rotation at the inlet which decays downstream. It was shown that with the increase in the inlet swirl intensity decay of swirl gets faster downstream and during this process the momentum carried by the tangential velocity is transferred to smaller scale turbulent structures. The appearence of turbulence and vortex breakdown support this assumption. Much of the energy carried by the tangential momentum is spent in the conservation of these turbulent structures which leads to the faster swirl decay. Numerical simulations studying the characteristics of swirl generated using the honeycomb have been carried out by Ayinde (2010); Najafi *et al.* (2005).

In order to find answer to some questions unanswered by the experiments (Genc *et al.*, 2009) and to validate the results, the present numerical study was carried out. Unlike experiments the numerical simulations provide a powerful tool to visualize the flow fields in detail and capture minute details like the different flow structures occuring due to the momentum transfer as mentioned above. The focus of the present study is to understand the decay of swirl and to visualize the flow structures. Due to some appealing similarities in their nature, these structures can be thought to be analogous with those obtained in the Taylor-Couette flows (Sprague & Weidman, 2009).

2. Numerical modeling

2.1. Flow domain
An unsteady, laminar, incompressible flow in a straight constant-diameter pipe is considered. Depending on the type of inlet swirl condition, two cases are studied in the following simulations. Case(I) involves the inlet swirl generated by a rotating honeycomb whereas Case(II) uses a tangential velcoity profile at the inlet such that a solid body rotation is imparted to the fluid by a constant angular velocity. The Case(II) serves as a comparison to analyze the swirl generated using the honeycomb and helps to find out whether the various effects observed are generated inside the honeycomb or after that.

For Case(I) the flow domain consists of three parts as shown in figure 1. The first part is the rotating pipe (ϕ= 50mm), followed by the rotating honeycomb and the stationary pipe. The honeycomb can be visualized as a bundle of pipes of small diameters (ϕ= 3.5mm) packed inside a circular pipe. The length to diameter ratio (L/D) of the stationary pipe is 20. The flow domain for Case(II) as illustrated in figure 1 just includes the stationary pipe with suitable inlet condition.

2.2. Mesh characteristics
An unstructured trimmed mesh with prism layer for resolving the boundary layer is generated using the mesher provided by STAR-CCM+$^{\copyright}$. The Case(I) has a mesh comprising 9 million cells. For Case(II) the mesh size is 2.3 million. The sections of the mesh for Honeycomb are shown in figure 2. While clustering of the grid near the wall it was ensured that the viscous sublayer is properly resolved.
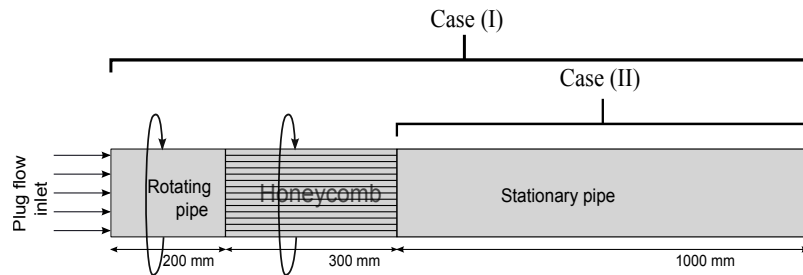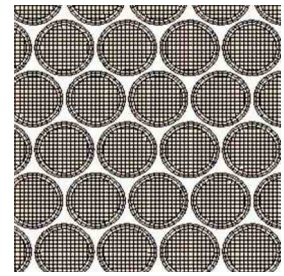
Figure 1: Computational domain.

Figure 2: Computational grid used in the honeycomb of Case(I).

2.3. Boundary conditions

For the Case(I) a plug flow profile with U_z=0.135 m/s is provided at the inlet of the rotating pipe. The swirl is introduced at the inlet of the stationary pipe by rotating the honeycomb with a constant angular velocity ω. On the other hand for Case(II) following inlet conditions are introduced: $U_\theta = r\ \omega$, U_r=0, $U_z = 0.135$ m/s. Hence, the Reynolds number for both cases is kept constant at 1730, which is well below the transition Reynolds number for pipe flows. The pressure outlet condition is used at the exit of the stationary pipe for both the cases. Radial equilibrium outflow is applied to the specified pressure boundary condition as:

$$p_f = p_i + \int_{r_i}^{r} \frac{\rho U_\theta{}^2}{r} dr \tag{1}$$

where the subscript i refers to the inner location and v_θ is the tangential component of the velocity. For the radial equilibrium outflow the radial pressure gradient exactly balances the centrifugal forces due to rotation. The no slip condition $u_i = 0$, wherever applicable was imposed at the pipe wall.

2.4. Test cases and methodology of solution

Swirling flow in general, as well as in a pipe, can be defined as a flow having a rotational velocity along with the linear velocity component. For swirl flows generated by solid-body rotation, as in the case under consideration, the swirl ratio N describes the amount of swirl at the inlet and is defined as

$$N = \frac{\Omega R}{U_{ave}} \tag{2}$$

where Ω is the angular velocity, R is the radius of the pipe and U_{ave} is the mean axial velocity. N is the definition used to quantify the swirl of solid body rotation locally at the inlet of the pipe. However as we move downstream of the pipe the swirl decays and the solid-body rotation disappears. For quantifying the swirl locally downstream of the pipe we use the parameter S, the swirl intensity. It is defined as the ratio of axial flux of tangential momentum to the axial flux of axial momentum times the effective nozzle radius.

$$S = \frac{\text{Axial flux of tangential momentum}}{\text{Axial flux of axial momentum} \cdot \text{Radius}} = \frac{2\pi \int_0^R \rho\, W\, U\, r^2\, dr}{R \cdot 2\pi \int_0^R \rho\, U^2\, r\, dr} \tag{3}$$

where, W is the tangential velocity, U the axial velocity and R is the radius of the pipe. Since S can be evaluated locally it can be used as a measure of local swirl downstream.

The definition of swirl as described in the above equations (2 and 3) has been used in the present work. The swirl numbers $N = 1, 2, 4.4, 8.8$ corresponding to $S = 0.5, 1, 2.2, 4.4$ respectively have been used in the present work. The swirl numbers are chosen in such a way as to encompass the sub-critical and super-critical swirl intensities. In literature different values can be found for the critical swirl intensity depending upon the inlet swirl condition and the observed nature of the flow. The value for S_{crit} ranges from 0.6 (Wiedemann, 2001) to 0.95 (Genc *et al.*, 2010).

The Direct numerical simulations (**DNS**) were carried out using commercial code STAR-CCM+$^{©}$ which solves the time-dependent Navier-Stokes equations using Finite volume method. The central- and upwind-differencing discretization schemes for space-discretization are used for Case(II) and Case(I) respectively. Similarly implicit Crank-Nicolson scheme which is second-order in time is used for time-discretization. The **SIMPLE** coupling algorithm (Patankar & Spalding 1972) using the velocity under-relaxation factors 0.7 and 1.0 for Case(I) and Case(II) respectively is implemented by the code to solve the equations numerically. In addition the rotating motion is imparted in Case(I) to the fluid in contact with the surfaces of the body by considering the actual displacement of mesh vertices in real time. All the above mentioned cases are simulated for a total of 17.6 s.

3. Results and discussions

The simulation results are validated with the experiments carried out using the similar experimental set-up by Genc *et al.* (2009, 2010). The analysis of the simulations are focusing on the characteristics of the swirl decay as obtained from the simulations and visualization of the corresponding vortex structures.

3.1. Comparison with the experiments

The flow profiles obtained from both the simulation cases are compared with the experiments carried out using the similar set-up by Genc *et al.* (2009, 2010). Figure 3 emphasizes the comparison between the axial and tangential velocity profiles obtained from the experiments and the simulations. It can be inferred from the various experimental data in the literature that the initially solid body rotation type vortex at the inlet converts itself to a Rankine type vortex. However this peculiarity of such flows is somehow not captured by the numerical simulations with Case(I). The turbulent intensities have been found to be extremely low. This indicates that the turbulent nature of the flow has not been captured by the simulations. This can be attributed to the fact that Case(I) was simulated using highly dissipative Upwind differencing scheme which damps any turbulence generated. The experiments on the other hand show turbulent velocity fluctuations. Also the transition from initial solid body type vortex to the Rankine type vortex is seen in the experiments. This is an evidence that turbulence structures are introduced in the flow due to the effect of swirl. Hence, the results discussed in the ongoing text predominantly include those obtained from Case(II).

Case(II) shows similarity to a large extent with the experiments. As shown in the tangential velocity profiles in figure 3 the solid-body to Rankine vortex transition is well captured. Also similar to the experiments, turbulent intensities are captured by the Case(II) simulations. These turbulent intensities are shown in figure 4 and figure 5.

3.2. Decay of swirl

It is already known that the swirl intensity introduced at the inlet decays downstream of the pipe. Depending on the intensity of the inlet swirl, different decay characteristics are observed. Figure 6 shows the time-averaged axial velocity contours as seen on the center plane section of the pipe. Figure 7 illustrates the drop in the time-averaged axial velocity at the center of
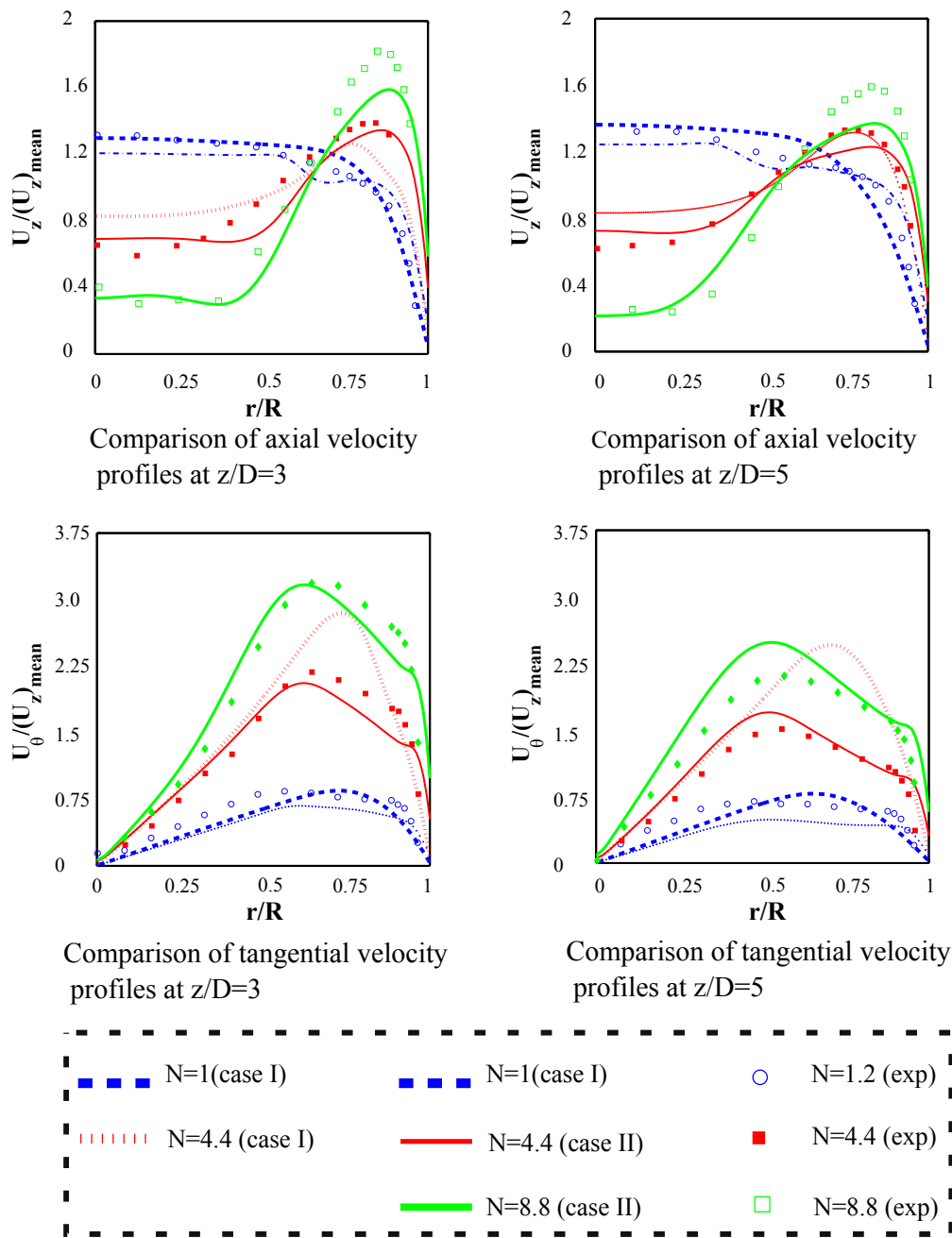
Figure 3: Comparison of the time-averaged velocity profiles with the experiments.

the pipe for higher swirl numbers. The tendency towards flow reversal starts at $N = 4.4$ and becomes more prominent at $N = 8.8$. Further increase in N can be thought to cause vortex breakdown designated by a flow reversal.

Similarly the time-averaged tangental velocity contours are shown in figure 8. The scale is normalized with the local tangential velocity at the inlet. It clearly illustrates that the solid body rotation at the inlet decays extremely faster for higher swirl intensities. Similar trend is observed next to the wall too. For $N=1$ the swirl persists for a longer distance downstream of the pipe before it dies out whereas for $N=8.8$ it subsides much earlier.

Turbulence intensity fields shown in figure 4 and figure 5 depict clearly that the turbulence
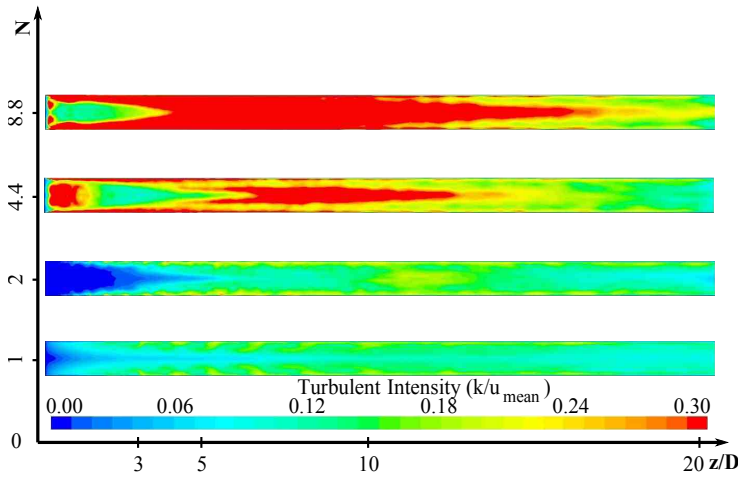
Figure 4: Time-averaged Turbulent intensity contours for various N (Case II).
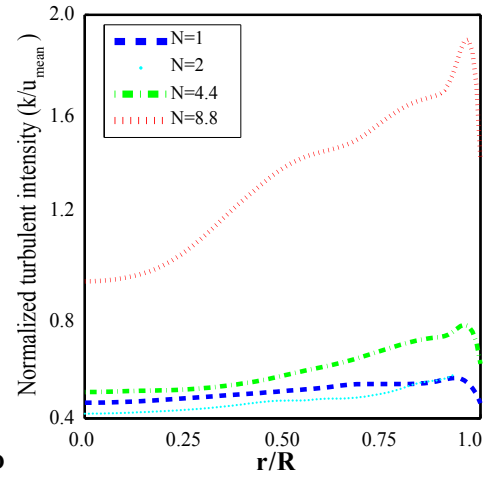
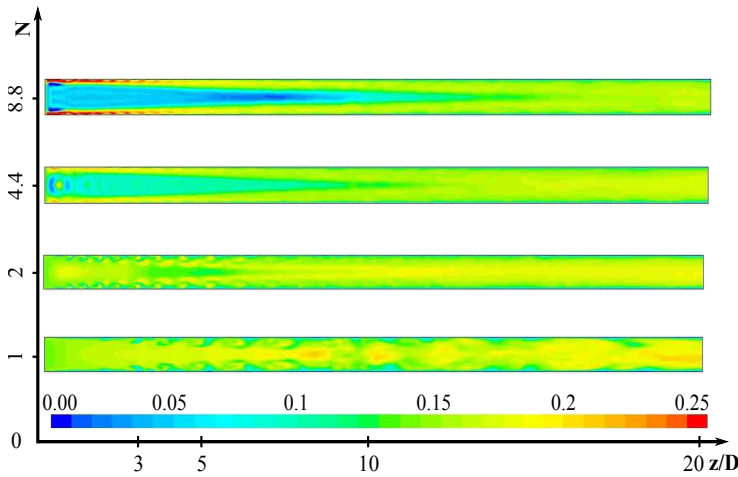Figure 5: Comparison of turbulent intensities for various N at z/D=3(Case II).

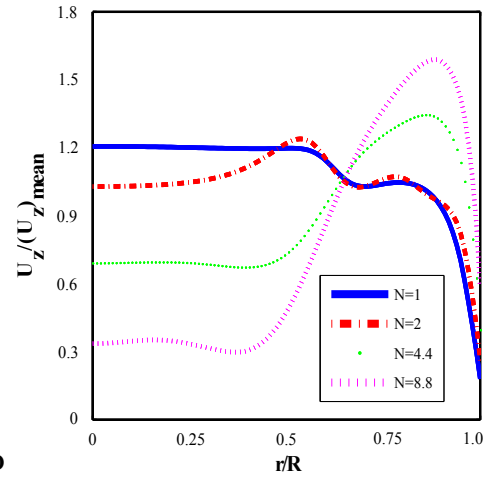Figure 6: Time-averaged axial Velocity contours for various N (Case II).

Figure 7: Comparison of axial velocity for various N at z/D=3(Case II).

starts at the wall for $N = 1$ and penetrates to the core for higher swirl numbers. In this way the momentum carried by the tangential velocity is transferred to the turbulent structures. This is also one of the reasons why the swirl decays faster at higher inlet swirl.

Figure 10 shows the decay of the inlet swirl intensities as observed in the experiments and simulations. As can be clearly seen, there is a deviation from the induced swirl at the inlet (indicated by Theo. Max in the figure). As the inlet swirl intensity increases, the deviation from the induced solid body rotation becomes more pronounced. The extent of deviation at higher swirl intensities indicates faster decay of swirl.

3.3. Flow structures
The swirling flow can be divided into a core region and an annular region, characterized by forced-vortex and free-vortex types, respectively (see tangential velocity profiles in figure 3. As the flow progresses downstream, the core region shrinks while the annular region of free vortex expands (Ayinde, 2010). As a result structures occur between the vortex-dominated core
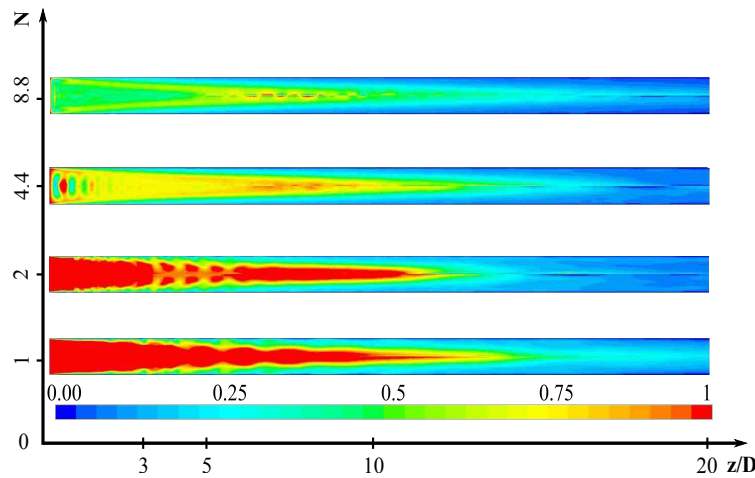
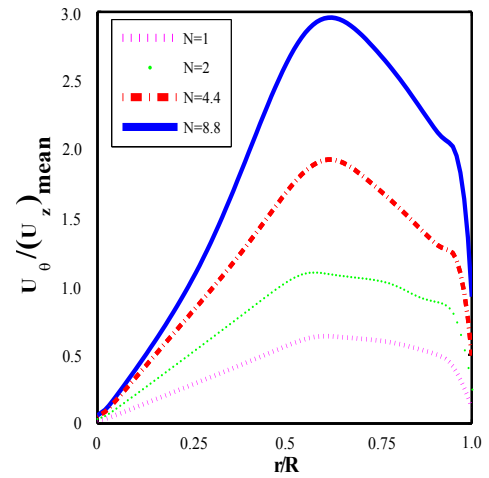Figure 8: Time-averaged tangential Velocity contours for various N (Case II).

Figure 9: Comparison of tangential velocity for various N at $z/D=3$(Case II).
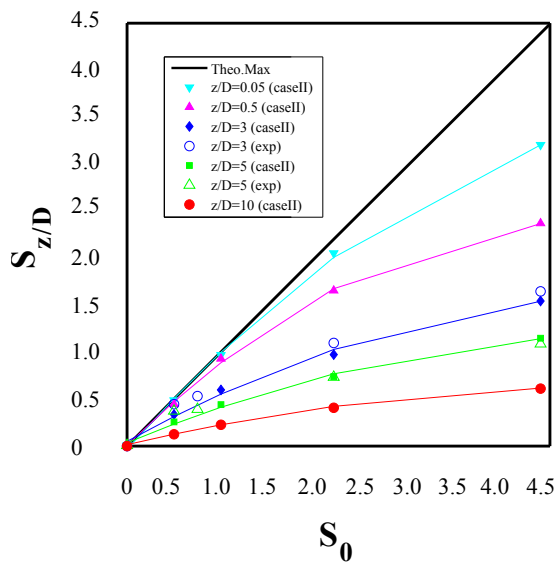

Figure 10: Inlet swirl intensity (So) vs. Measured/Simulated swirl intensity at several z/D. Solid lines represent the trendlines of the simulations.

region and the strain-dominated outer wall region. The structures are first observed in the radial velocity component as shown in figure 11. In this figure one pair of adjacent positive and negative regions (shown by red and blue colour respectively) form a vortical structure. Radial velocity component being the weakest shows the maximum fluctuations. It plays an important role in the momentum transfer from the core to the wall and vive-versa. The occurrence of structures between a rotating inner cone and a stationary outer cylinder in Taylor-Couette flows has been illustrated by Sprague & Weidman (2009). From the simulations it has been observed that the flow consists of a solid-body rotation at the inlet which disappears gradually downstream of the pipe. This creates a tapering core which is rotating with the inlet rotation speed. Thus this is similar to the arrangement as described by Sprague & Weidman (2009). As a result the structures so obtained are found to be analogous to those obtained in the Taylor-Couette flows. Figure 12 displays the sections at various z/D positions. Here we can clearly see the number and distribution of these structures. These structures disappear at $N = 4.4$ and again reappear at $N = 8.8$.
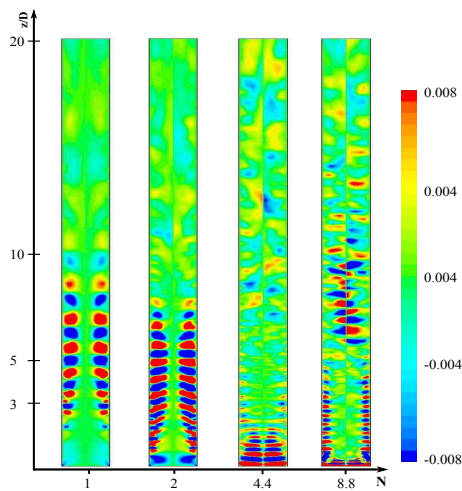
Figure 11: Time-averaged radial velocity contours for various N (Case II).
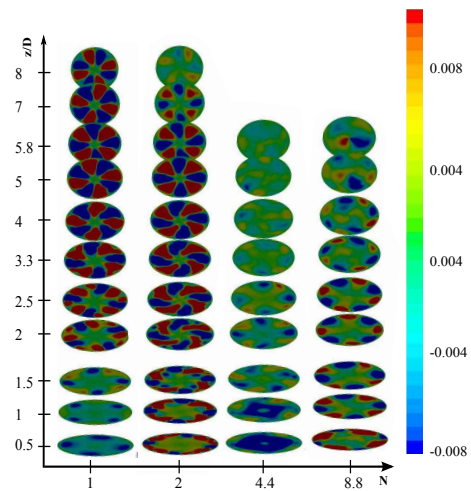

Figure 12: Time-averaged radial velocity profiles at different x-y planes for various N. (Case II)

Similarly figure 13 shows the helicity profiles for different N. The concept of normalized helicity, as introduced by Levy (1990), is used here for detecting vortex cores. It is the cosine of the angle between velocity($\mathbf{v}$) and vorticity(ω) . It makes use of the fact that near vortex core regions, the angle between $\mathbf{v}$ and ω is small. Its sign indicates the direction of swirl (clockwise or counterclockwise) of the vortex with respect to the streamwise velocity component (Jiang *et al.*, 2004).

$$H_n = \frac{v \cdot \omega}{|v||\omega|} \tag{4}$$

It can be observed that $H_n = 1$ at the core region which indicates that the vorticity is in the same direction as the flow velocity. However this region shrinks with increasing N. Hence, as the swirl intensity increases, the vorticity is less aligned with the flow velocity. The structures observed in the wall region are the centers of vortices rotating in the counter-clockwise direction. These structures appear to be analogous with those seen in the radial velocity profiles. Figure 14 elaborates the above mentioned vortex structures

Various streamlines describing the nature of the flow are shown in figure 15. The seeding is done at positions on a x-y plane where the H_n=-1. The streamlines exhibit helical nature which is common to such kind of flows. As N increases the pitch of these helical streamlines decreases. The scale on the right corresponds to the x-y section and the colored streamlines are used just to differentiate them. At higher N the core of the structures are not preserved. Hence the streamlines disperse very fast downstream of the pipe inlet.

4. Conclusions

Conducted numerical simulations confirmed the observed turbulence and fast decay of Swirl intensity in the experiments. Helical vortices are visualized between the conical core having a solid body rotation and the pipe wall. These structures are analogous to those observed in Taylor-Coutte flows with tapered inner cylinder.
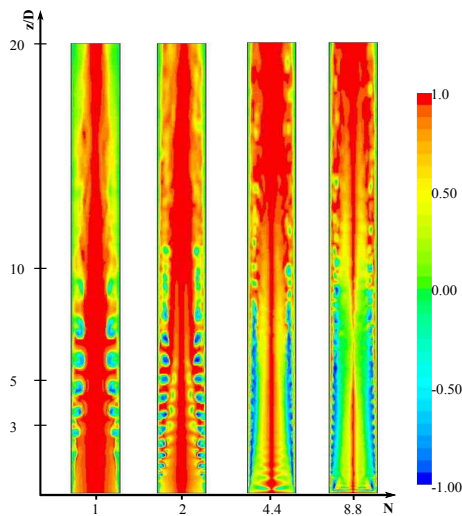
Figure 13: Normalized time-averaged helicity contours for various N (Case II).
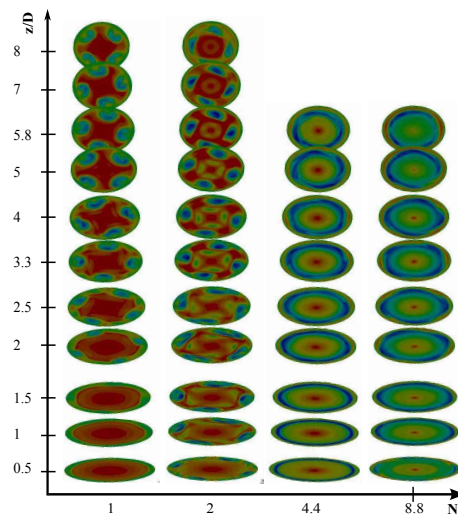

Figure 14: Normalized time-averaged helicity profiles at different x-y planes for various N. (Case II)
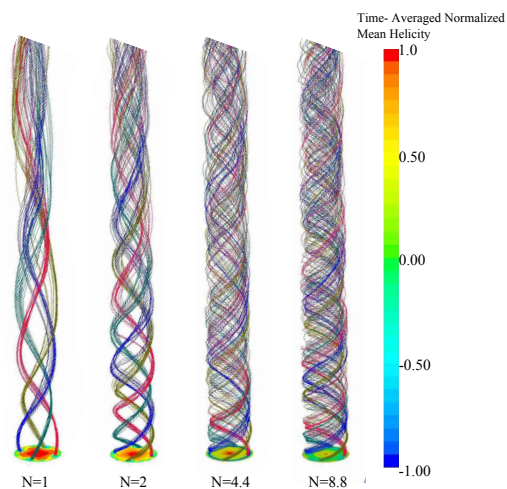

Figure 15: Flow streamlines (Case II) (seeding is done at locations on a particular x-y plane where time-averaged H_n=-1.)

Acknowledgments

References

AYINDE, T. 2010 A generalized relationship for swirl decay in laminar pipe flow. *Sadhana* **35**, 129–137.

BILLANT, P. & CHOMAZ, J-M. & HUERRE, P. 1998 Experimental study of vortex breakdown in swirling jets. *J. Fluid Mech.* **376**, 183–219.

FACCIOLO, L. & TILLMARK, N. & TALAMELLI, A. & ALFREDSSON, H. P. 2007 A study of swirling turbulent pipe and jet flows. *Physics of Fluids* **19**, 035105–035122.

Genç, B. Z. , Ertunç, Ö. , Jovanovic, J. , Delgado, A. 2009 LDA Measurements of Reynolds stresses in a swirling turbulent pipe flow. *European Turbulence Conference 12, Marbug*.

Genç, B. Z. , Ertunç, Ö. , Vaidya, H. A. , Köksoy, Ç. , Delgado, A. 2010 On the increased decay of swirl after vortex breakdown. *Bull. Am. Phy. Socy.*, **55**, 16.

Genç, B. Z. , Jovanovic, J. , Durst, F. 2005 LDA Measurements in a Strongly Swirling Pipe Flow. *GALA Fachtagung:Lasermethoden in der Strmungsmechanik* .

Jakirlic, S. & Hanjalic, K. & Tropea, C. 2007 Modeling rotating and swirling turbulent flows: a Perpetual challenge. *AIAA Journal* 1984–1996.

Jiang, M. & Machiraju, R. & Thompson, D. 2004 Detection and Visualization of Vortices. In *Visualization Handbook* (ed. Johanson, C. R. & Hansen, C. D.), pp. 295–297. CiteSeer.

Kito, O. 1984 Axi-asymmetric Character of Turbulent Swirling Flow in a Straight Circular Pipe. *JSME, Bulletin* **27**, 683–690.

Kitoh, O. 1991 Experimental Study of Turbulent Swirling Flow in a Straight Pipe. *J. Fluid Mech.* **225**, 445–479.

Leibovic, S. The structure of vortex breakdown. *Annual Review of Fluid Mechanics* **10**, 221–246.

Levy, Y. & Degani, D. & Seginer, A. 1990 Graphical visualization of vortical flows by means of helicity. *AIAA Journal* **28**, 1347–1352.

Lucca-Negro, O. & Doherty & T. O. 2001 Vortex breakdown: a review. *Progress in Energy and Combustion Science* **27**, 431–481.

Najafi, A. F. & Saidi & M. H. & Sadhegipour, M. S. & Souhar, M. 2005 Numerical analysis of turbulent swirling decay pipe flow. *International Communications in Heat and Mass Transfer* **32**, 627–638.

Nishibory, K. & Kikuyama, K. & Murakami, M. 1987 Laminarization of Turbulent Flow in the Inlet Region of an Axially Rotating Pipe. *J. Fluid Mech.* **30**, 255–262.

Novak, F. & Sarpkaya, T. 2000 Turbulent vortex breakdown at high reynolds numbers Pipe Flow. *AIAA Journal* **38**, 825–834.

Pashtrapanska, M. & Jovanovic, J. & Lienhart, H. & Durst.F 2006 Turbulence measurements in a swirling pipe flow. *Experiments in Fluids* **41**, 813–827.

Patankar, S. V. & Spalding, D. B. 1972 A calculation procedure for heat, mass and momentum transfer in three-dimensional parabolic flows. *International Journal of Heat and Mass Transfer* **15**, 1787–1806.

Rocklage-Marliani, G. & Schmidts, M. & Vasanta Ram, V. I H. 2003 Three-dimensional laser-doppler velocimeter measurements in swirling turbulent pipe flow. *Flow, Turbulence and Combustion* **46**, 43–67.

Steenbergen, W. 1995 Turbulent pipe flow with swirl. PhD thesis, Eindhoven University of Technology.

Sprague, M. A. & Weidman, P. D. 2009 Continuously tailored Taylor vortices. *Physics of Fluids* **21**, 114106–114113.

Syred, N. & Beer, J. M. 1972 Combustion in swirling flows: A review. *Combustion and Flame* **2**, 143–201.

Wiedemann, A. 2001 Mehrkomponenten-Laser-Doppler-Anemometer-Messungen in einer drallbehafteten Rohr- und Brennkammerstrmung. PhD thesis, Georg-August-Universität zu Göttingen.